MOCVD growth of β-phase $(Al_xGa_{1-x})_2O_3$ on $(\bar{2}01)$ β-Ga_2O_3 substrates

A F M Anhar Uddin Bhuiyan[1], Zixuan Feng[1], Jared M. Johnson[2], Hsien-Lien Huang[2], Jinwoo Hwang[2], and Hongping Zhao[1,2,a)]

[1]*Department of Electrical and Computer Engineering, The Ohio State University, Columbus, OH 43210, USA*

[2]*Department of Materials ScieSnce and Engineering, The Ohio State University, Columbus, OH 43210, USA*

[a)]Corresponding author Email: zhao.2592@osu.edu

β-$(Al_xGa_{1-x})_2O_3$ thin films are grown on $(\bar{2}01)$ β-Ga_2O_3 substrates via metal organic chemical vapor deposition to investigate the solubility of Al in β-phase Ga_2O_3. The X-ray diffraction (XRD) spectra reveal crystalline quality $(\bar{2}01)$ β-$(Al_xGa_{1-x})_2O_3$ thin films with Al compositions up to 48%. The Al compositions are further confirmed by high resolution X-ray spectroscopy measurement and energy-dispersive X-ray spectra (EDS) mapping. The bandgap energies extracted from XPS spectra range between 5.20 ± 0.06 eV and 5.72 ± 0.08 eV for x = 21% - 48%. The surface morphology evaluated by both scanning electron microscopy (SEM) and atomic force microscopy shows elongated features with granules along the [010] direction, which are suppressed with increasing Al content. A systematic growth study through tuning growth parameters indicates that the chamber pressure plays an important role on both surface morphology and Al incorporation. Material characterization via high resolution scanning transmission electron microscopy (HRSTEM) and STEM-EDS reveal Al fluctuations in the sample with 48% Al composition. Atomic resolution STEM imaging and XRD spectra for $(\bar{2}01)$ β-$(Al_xGa_{1-x})_2O_3/Ga_2O_3$ superlattice structures confirm the periodicity of the β-$(Al_xGa_{1-x})_2O_3/Ga_2O_3$ sub-layers is well maintained with high-Al compositions.

Keywords: ultrawide bandgap, $(\bar{2}01)$ β-$(Al_xGa_{1-x})_2O_3$ thin films, metalorganic chemical vapor deposition, superlattice structures

β-Ga_2O_3 has attracted a great attention for power electronics due to its large energy bandgap (~4.85 eV) and controllable n-type doping [1-7]. Significant progresses, since its first conceptual device demonstration [5, 8], have been made in the development of native substrates [9-11], thin film epitaxy [2-4, 12, 13] and electronic devices [8, 14-21]. Commercially available high quality and scalable β-Ga_2O_3 substrates in different crystal orientations, such as (010), (001), ($\bar{2}$01) and (100), provide opportunities of developing and understanding Ga_2O_3 and AlGaO materials and devices [22].

High quality β-Ga_2O_3 thin films and devices have been demonstrated on (010) Ga_2O_3 substrates via molecular beam epitaxy (MBE) [13], metal organic chemical vapor deposition (MOCVD) [2-4], and low pressure chemical vapor deposition (LPCVD) [12, 23]. Halide vapor phase epitaxy (HVPE) selected (001) Ga_2O_3 as a preferred growth orientation for thick films [24]. MOCVD growth of (100) β-Ga_2O_3 was studied comprehensively [25]. Among the various crystal orientations, ($\bar{2}$01) substrates have attracted a great deal of attention due to their availability in large sizes. However, recent MBE growth studies of ($\bar{2}$01) β-Ga_2O_3 films on ($\bar{2}$01) Ga_2O_3 substrates have revealed degraded structural quality with the formation of twin defects which are suggested to be mitigated by optimizing the growths conditions and by using offcut substrates [26-28].

Despite the successful growth efforts on β-Ga_2O_3, reports involving the alloying of Ga_2O_3 with Al_2O_3 have been limited. The solubility limit of β-$(Al_xGa_{1-x})_2O_3$ is not well understood, although equilibrium phase diagram predicted the maximum solubility of Al_2O_3 in Ga_2O_3 can be as high as ~67% [29]. Following the success of nitride based high electron mobility transistors (HEMTs) and arsenide based modulation doped field effect transistors (MODFETs), modulation doping in β-$(Al_xGa_{1-x})_2O_3$/Ga_2O_3 heterostructures with Al composition of 18-20% have been

demonstrated [30, 31]. Achieving β-$(Al_xGa_{1-x})_2O_3$ with high-Al composition is advantageous as it enables to form large heterostructure band offset with high 2DEG sheet charge concentration, which is predicted to screen phonon scattering and enhance carrier mobility [32].

The challenge to develop high quality β-phase $(Al_xGa_{1-x})_2O_3$ with high-Al composition is due to 1) increase of lattice-mismatch between $(Al_xGa_{1-x})_2O_3$ and Ga_2O_3 as x increases; 2) different sticking coefficient between Al and Ga on the growth surface; and 3) increase of defects concentrations as the $(Al_xGa_{1-x})_2O_3$ energy bandgap widens. Thus far, the maximum Al incorporation in β-$(Al_xGa_{1-x})_2O_3$ along (010) growth orientation is ~27% [33, 34]. As x increases, phase segregation appears regardless of the epitaxial growth method [35, 36]. As for β-$(Al_xGa_{1-x})_2O_3$ grown along the (100) orientation, up to 61% and 52% Al were demonstrated via MBE [37] and MOCVD [38]. Epitaxy development of β-$(Al_xGa_{1-x})_2O_3$ on $(\bar{2}01)$ Ga_2O_3 substrates is still lacking.

In this letter, MOCVD growths of β-$(Al_xGa_{1-x})_2O_3$ thin films on $(\bar{2}01)$ β-Ga_2O_3 substrates were investigated. By systematic mapping of the growth parameters including precursor flow rate, chamber pressure and growth temperature, Al incorporation up to 48% in pure β-phase $(Al_xGa_{1-x})_2O_3$ films was demonstrated. Coherent growth of $(\bar{2}01)$ β-$(Al_xGa_{1-x})_2O_3/Ga_2O_3$ superlattice structures with various Al compositions was achieved. Comprehensive characterization via X-ray diffraction (XRD, Bruker D8 Discover), high resolution scanning transmission electron microscopy (HRSTEM, Thermo Fisher Scientific Titan and Themis Z) imaging, energy dispersive X-ray spectroscopy (EDS) mapping, scanning electron microscopy (SEM, FEI Helios 600), and atomic force microscopy (AFM, Bruker ICON) have revealed phase pure epitaxy of $(\bar{2}01)$ β-$(Al_xGa_{1-x})_2O_3$ films and $(\bar{2}01)$ β-$(Al_xGa_{1-x})_2O_3/Ga_2O_3$ superlattice (SL)

structures with Al compositions close to 50%. Al compositions and energy bandgaps were further extracted from X-ray photoelectron spectroscopy (XPS, Kratos Axis Ultra XPS). The binding energy scale was referenced to C 1s core level (284.8 eV).

Commercially acquired Sn doped $(\bar{2}01)$ β-Ga_2O_3 substrates (NCT, Inc.) were used for MOCVD growth. High temperature (920 °C) in-situ annealing under O_2 atmosphere was employed for 10 minutes prior the $(Al_xGa_{1-x})_2O_3$ growth. Trimethylaluminum (TMAl), Triethylgallium (TEGa) and pure O_2 were used as Al, Ga and O precursors, respectively. Argon was used as the carrier gas. The explored growth window includes a varying chamber pressure between 20 and 80 torr, growth temperature between 880 and 920 °C, constant O_2 flow rate of 500 sccm, and [TMAl]/[TMAl+TEGa] molar flow rate ratio between 2.35% to 18.08%.

The XRD 2θ-ω spectra for $(\bar{4}02)$ and $(\bar{6}03)$ reflections of β-$(Al_xGa_{1-x})_2O_3$ films with x = 21%, 29%, 36%, 41% and 48% are plotted in Fig. 1. All films were grown on β-Ga_2O_3 substrates at 880 °C and 20 torr with thicknesses estimated between 155 nm and 197 nm as listed in Table 1. The general trend shows that the film thicknesses increase with increasing [TMAl]/[TMAl+TEGa] molar flow rate ratio. XRD peaks at 2θ = 38.44° and 2θ = 59.18° correspond to the $(\bar{4}02)$ and $(\bar{6}03)$ crystal planes of β-Ga_2O_3 substrates, respectively. By varying the [TMAl]/[TMAl+TEGa] molar flow rate ratio from 2.35% to 18.08%, β-$(Al_xGa_{1-x})_2O_3$ films with increasing Al up to 48% were demonstrated based on the shift of both $(\bar{4}02)$ and $(\bar{6}03)$ peaks, using Vegard's law [39, 40].

High resolution XPS measurements on the series of β-$(Al_xGa_{1-x})_2O_3$ samples were performed to verify the Al compositions and to extract the energy bandgaps. Wide survey scans in the binding energy range 0-1200 eV for β-$(Al_xGa_{1-x})_2O_3$ films with different Al compositions were performed. Figure S1 in the supplementary material shows a survey scan spectrum for a

representative ($\bar{2}01$) β-$(Al_{0.48}Ga_{0.52})_2O_3$ sample. The XPS peaks for Ga, Al and O are identified, without other metallic contaminants. The insets of Fig. S1 plot the high resolution XPS spectra of Ga 3s and Al 2s core levels for β-$(Al_xGa_{1-x})_2O_3$ films with different Al compositions (x = 21%, 28%, 35%, 41% and 48%). The Al compositions were determined using Al 2s and Ga 3s core level peak areas and their corresponding relative sensitivity factors [37], which agree well with the values extracted from XRD listed in Table 1.

The energy bandgaps of the β-$(Al_xGa_{1-x})_2O_3$ films were characterized by XPS through analyzing the inelastic collisions that occur during photoexcitation and photoemission of electrons. Utilizing the energy loss peak of O 1s spectrum to estimate the energy bandgap for various wide bandgap semiconductors has been demonstrated previously [41-44]. Figure 2 shows the O 1s core level peaks for β-$(Al_xGa_{1-x})_2O_3$ films with x = 21%, 28%, 35%, 41% and 48%. Energy bandgap values were extracted from the difference of the onset of the inelastic loss spectra and the O 1s core level peak energy: 5.20 ± 0.06 eV (β-$(Al_{0.21}Ga_{0.79})_2O_3$), 5.35 ± 0.04 eV (β-$(Al_{0.28}Ga_{0.72})_2O_3$), 5.44 ± 0.08 eV (β-$(Al_{0.35}Ga_{0.65})_2O_3$), 5.54 ± 0.05 eV (β-$(Al_{0.41}Ga_{0.59})_2O_3$), and 5.72 ± 0.08 eV (β-$(Al_{0.48}Ga_{0.52})_2O_3$). These results match well with the theoretically predicted energy bandgap values for β-$(Al_xGa_{1-x})_2O_3$ [39].

FESEM and AFM imaging were used to characterize the surface morphology of β-$(Al_xGa_{1-x})_2O_3$ samples. Figures S2 (a)-(d) in the supplementary material show the surface view FESEM images of β-$(Al_xGa_{1-x})_2O_3$ films with x = 21%, 29%, 41%, and 48%, respectively. Samples with relatively low Al composition exhibit elongated surface morphology with granules along the [010] direction as shown in Figs. S2 (a, b). β-gallia structure has two cleavage planes that are parallel to the [100] and [001] directions [37]. Due to the higher surface energy of (010) plane as compared to those of the (100) and (001) planes [25], the adatom incorporation along the

[010] direction is thus higher, causing the directional growth toward the [010] direction [28]. The similar granular surface morphology was previously observed in MBE grown ($\bar{2}01$) β-Ga_2O_3 films [28]. With increasing Al composition, the granular surface feature size reduces as shown in supplementary Fig. S2. This trend indicates that the surface morphology of ($\bar{2}01$) β-$(Al_xGa_{1-x})_2O_3$ films highly depends on the Al composition.

AFM images (5 x 5 μm^2) in Fig. 3(a)-(d) were taken for the samples shown in Fig. S2. The surface morphology and root mean square (RMS) roughness show an obvious trend as Al composition increases. For β-$(Al_xGa_{1-x})_2O_3$ films with x = 21% and 29% [Figs. 3(a) and 3(b)], surfaces exhibit granular morphology with lengths of 1.0-1.2 μm, oriented along the [010] direction. The RMS values were measured at 7.13 nm and 9.71 nm, respectively. As the Al composition increases to 41% and 48% [Figs. 3(c) and 3(d)], the lengths of the granule structures reduce to ~ 0.4-0.55 μm with better uniformity and RMS of 5.37 nm and 4.28 nm. While recent MBE growth of ($\bar{2}01$) β-Ga_2O_3 films have correlated the reduction of RMS roughness with growth temperature [28], from the MOCVD growth of ($\bar{2}01$) β-$(Al_xGa_{1-x})_2O_3$, we observed that the RMS value tends to decrease with Al increases under the same growth temperature (880°C) and pressure (20 torr). The introduction of Al adatoms to the growth surface can facilitate uniform nucleation on the ($\bar{2}01$) surface, due to a higher sticking coefficient of Al than Ga [45] and stronger Al-O bonding energy than Ga-O [46]. With higher flow rate of TMAl, the dense Al adatoms can act as preferential nucleation sites, which promotes epitaxy with uniform surface morphologies.

MOCVD growth condition was tuned to investigate its impact on the β-$(Al_xGa_{1-x})_2O_3$ film crystalline quality and surface morphology. Three samples were grown with varied chamber pressure and temperature, but with the same [TMAl]/[TMAl+TEGa] molar flow rate ratio of

3.82%. Figure 4(a) compares the XRD spectra for the three films grown at (i) 880 °C and 80 torr, (ii) 920°C and 20 torr, and (iii) 880°C and 20 torr. As the growth pressure increases from 20 to 80 torr at the same temperature (880°C), the shift of the ($\bar{6}$03) refection peak indicates a reduction of Al composition from 29% to 25%. From our previous study on the MOCVD β-Ga_2O_3, the gas phase reaction between MO sources and oxygen becomes more severe as growth pressure increases [2], which leads to the reduction of Al incorporation. Comparing Fig. 4(c) and Fig. S2(b) in the supplementary material, surface morphologies show obvious change that the granule feature size reduces at the higher growth pressure. Although higher Al incorporation at the same chamber pressure (20 Torr) can lead to surface smoothening as shown in supplementary Fig. S2, we observed that the higher chamber pressure can also promote the epitaxial growth with smoother surface morphologies. While the chamber pressure has a strong influence on the Al incorporation and the surface morphology, the increase of growth temperature from 880 to 920 °C does not show obvious impact on XRD peak position or surface morphology (Fig. 4(b)).

The crystalline quality and the alloy homogeneity of high Al content ($\bar{2}$01) β-$(Al_xGa_{1-x})_2O_3$ films were evaluated at the atomic scale by high-angle annular dark-field (HAADF) STEM imaging and EDS. HAADF STEM images, shown in Figs. 5(a) and (b), display the ($\bar{2}$01) β-$(Al_{0.48}Ga_{0.52})_2O_3$ film grown on a ~65 nm ($\bar{2}$01) β-Ga_2O_3 buffer layer. As HAADF signal is approximately proportional to the square of an elements atomic number [47], the contrasts in the images directly correspond to Al incorporation and segregation, producing darker regions in the film as compared to the brighter β-Ga_2O_3 substrate. The low magnification image, shown in Fig 5(a), reveals a 60 nm thick film on top of a β-Ga_2O_3 substrate, which is clearly visible by locating the sharp interface. We note that the interface between the ~65 nm UID ($\bar{2}$01) β-Ga_2O_3 buffer layer and the β-Ga_2O_3 substrate was not clearly identified, which indicates good quality homoepitaxial

growth of the $(\bar{2}01)$ β-Ga_2O_3 buffer layer. Additionally, as seen in Fig. 5(a), the significant contrast observed in the $(Al_xGa_{1-x})_2O_3$ film indicates an inhomogeneous Al distribution. This contrast is also detected at the atomic scale, where atomic column intensity fluctuates as a result of non-uniform Al distribution (Fig. 5(b)). Elemental maps for Ga and Al, shown in Figs. 5(c) and (d), indicate that the darker regions of the film in Fig. 5(a) arise from the increase in Al concentration. Furthermore, the EDS quantitative line scan (orange arrow), plotted in Fig. 5(e), shows the fluctuation of Al concentration in the film with experimental uncertainty of ~±5%, which is typical for EDS. Still, the EDS quantified average Al composition matches well with the calibrated Al composition of 48%. The exact Al distribution pattern, seemingly align with the [100] direction, which is parallel to the (100) primary cleavage plane in β-Ga_2O_3. This directional dependence of the Al distribution along [100] direction in the $(\bar{2}01)$ β-$(Al_xGa_{1-x})_2O_3$ layer can be the consequence of the highly anisotropic properties of β-gallia structure.

Unlike (010) β-$(Al_xGa_{1-x})_2O_3$ films grown on (010) β-Ga_2O_3 substrates, where the Al incorporation in pure β-phase is found to be limited ($x < 27\%$) due to the domain rotation and phase segregation while targeting for high-Al compositions [35], $(\bar{2}01)$ β-$(Al_xGa_{1-x})_2O_3$ films grown on $(\bar{2}01)$ β-Ga_2O_3 substrates do not exhibit any domain rotation or phase segregations even at high-Al compositions. We believe this can be related to the asymmetric crystal structures of β-$(Al_xGa_{1-x})_2O_3$. The lattice constants a, b, and c for the monoclinic β-Ga_2O_3 structure are 1.22 nm, 0.30 nm, and 0.58 nm, respectively [39]. This indicates the highly asymmetric bonding strength along with different crystal orientations. Among the major crystal surfaces of β-gallia structures including (010) and (001), the $(\bar{2}01)$ surface is more stabilized as the relaxation energy for $(\bar{2}01)$ is significantly larger than that for (010) or (001) surfaces. This leads to a lower surface energy of the relaxed $(\bar{2}01)$ plane (0.96 J/m^2) as compared to the surface energies of (010) [1.67 J/m^2] and

(001) [1.95 J/m^2] [48]. This significantly lower surface energy of ($\bar{2}$01) plane may lead to the higher Al adatom incorporations on the growth surface in pure β-phase without occurring any structural phase change or domain rotation. Comparing to our recent study on (100) β-$(Al_xGa_{1-x})_2O_3$ films grown on (100) β-Ga_2O_3 substrates [38], we also achieved phase pure β-$(Al_xGa_{1-x})_2O_3$ films with up to 52% Al compositions, which can be related to even lower surface energy of (100) surface planes (0.34 J/m^2) [48].

In addition to the growths of thin films, 8-period ($\bar{2}$01) β-$(Al_xGa_{1-x})_2O_3$/β-Ga_2O_3 SL structures with Al composition of 48% and 21% were investigated, which were grown on a ~65 nm β-Ga_2O_3 buffer layer (Fig. S3 in the supplementary material). The structural quality of the superlattice structures were evaluated by XRD and HRSTEM imaging. The periods consisting of β-Ga_2O_3 well and β-$(Al_xGa_{1-x})_2O_3$ barrier layers for 48% and 21% Al compositions targeted for 15 nm and 20 nm, respectively. The XRD spectrum, as shown in Fig. S3 in the supplementary material, shows distinguishable satellite peaks along with 0th order peak for both structures, indicating the periodicities of the structures are well maintained even with high-Al compositions. In general, the separation between β-Ga_2O_3 substrate peak and the 0th order satellite peaks reflects the average Al composition over the entire superlattices and the thickness of the period of the well and barrier [47, 49]. With increasing Al compositions, the 0th order satellite peaks shift towards higher 2θ angle, showing the increase of the average Al in the SL. For 48% Al SL, the average Al composition calculated from the distance between the substrate peak and 0th order satellite peak positions is 15% [targeted average Al%: (AlGaO barrier thickness: 5nm)/(GaO+AlGaO period thickness:15nm) x 48% = 16%] and the period thickness estimated from the separations between the adjacent satellite peak positions is 14.2 nm (targeted period: 5 nm+10 nm = 15 nm). Similarly, the average Al composition and the period for the SL structures with 21% Al are 9.5% (targeted

average Al%: 10.5%) and 21.26 nm (targeted period: 20 nm), respectively. The slight deviations between targeted and the extracted average Al compositions and the periods are observed which can be related to the Al inhomogeneity and the extent of interface abruptness due to the interdiffusion of Al and Ga across the interfaces.

To evaluate the interface abruptness and Al uniformity in the β-$(Al_xGa_{1-x})_2O_3$/β-Ga_2O_3 SL, HRSTEM imaging and EDS were performed. Figures 6(a-b) show HAADF-STEM images at low magnification and atomic resolution, respectively, of the SL structure grown with a target of 48% Al. The alternating dark and bright contrast in Fig. 6(a) corresponds to the β-$(Al_xGa_{1-x})_2O_3$ barriers and β-Ga_2O_3 wells. As shown in Figs. 6(c-d), STEM-EDS displays the relatively consistent Al concentration in the layered structure, but also the deterioration of the interfacial abruptness and inhomogeneous Al distribution within individual layers. The Al compositions in the $(Al_xGa_{1-x})_2O_3$ layers as determined by the quantitative line scan (orange arrow) shown in Fig. 6(e), show some deviation from the targeted Al composition (48%), which can be related to the nonuniform distribution of Al in $(Al_xGa_{1-x})_2O_3$ barrier layers.

In summary, MOCVD of $(\bar{2}01)$ β-$(Al_xGa_{1-x})_2O_3$ films on β-Ga_2O_3 substrates with up to 48% Al were investigated. Elongated surface morphology with granules along the [010] direction was observed, and the feature size reduces as Al composition increases. A mechanism for smoother surface morphology of β-$(Al_xGa_{1-x})_2O_3$ films with higher Al incorporation is proposed considering Al adatoms act as preferential nucleation sites promoting uniform surface morphologies. The Al incorporations and the surface morphologies are found to be greatly influenced by growth parameters, especially by the chamber pressure. In the $(\bar{2}01)$ β-$(Al_{0.48}Ga_{0.52})_2O_3$ film, although nonuniform distribution of Al composition is observed, the material maintains beta-phase and the SL structure suggests the promise to fabricate $(\bar{2}01)$ β-$(Al_xGa_{1-x})_2O_3$/Ga_2O_3 heterostructures with

high-Al composition. For future device applications, the challenge of nonuniform distribution of Al in films with high-Al needs to be addressed. One possible approach is to use off-axis ($\bar{2}$01) β-Ga_2O_3 substrates.

See the supplementary material for high resolution XPS spectra, surface view FESEM images for different Al composition films and XRD ω-2θ scan profiles and the schematic of eight-period ($\bar{2}$01) β-$(Al_xGa_{1-x})_2O_3$/β-Ga_2O_3 superlattice structures.

Acknowledgements

The authors acknowledge the Air Force Office of Scientific Research FA9550-18-1-0479 (AFOSR, Dr. Ali Sayir) for financial support. The authors also acknowledge the National Science Foundation (Grant No. 1810041, No. 2019753) for partial support. Electron microscopy was performed at the Center for Electron Microscopy and Analysis at The Ohio State University.

Data Availability

The data that support the findings of this study are available from the corresponding author upon reasonable request.

References:

1. M. Higashiwaki and G. H. Jessen, Appl. Phys. Lett. 112, 060401 (2018).
2. Z. Feng, A F M A. U. Bhuiyan, M. R. Karim, and H. Zhao, Appl. Phys. Lett. 114, 250601 (2019).
3. F. Alema, Y. Zhang, A. Osinsky, N. Valente, A. Mauze, T. Itoh, and J. S. Speck, APL Mater. 7, 121110 (2019).

4. Z. Feng, A F M A. U. Bhuiyan, Z. Xia, W. Moore, Z. Chen, J. F. McGlone, D. R. Daughton, A. R. Arehart, S. A. Ringel, S. Rajan, and H. Zhao, Phys. Status Solidi RPL. 14, 2000145 (2020).
5. M. Higashiwaki, K. Sasaki, A. Kuramata, T. Masui, and S. Yamakoshi, Appl. Phys. Lett. 100, 013504 (2012).
6. N. Ma, N. Tanen, A. Verma, Z. Guo, T. Luo, H. Xing, and D. Jena, Appl. Phys. Lett. 109(21), 212101 (2016).
7. J. L. Hudgins, G. S. Simin, E. Santi, and M. A. Khan, IEEE Trans. Power Electron. 18, 907 (2003).
8. M. Higashiwaki, K. Sasaki, T. Kamimura, M.H. Wong, D. Krishnamurthy, A. Kuramata, T. Masui, and S. Yamakoshi, Appl. Phys. Lett. 103, 123511 (2013).
9. N. Suzuki, S. Ohira, M. Tanaka, T. Sugawara, K. Nakajima, and T. Shishido, Phys. Status Solidi C 4, 2310 (2007).
10. H. Aida, K. Nishiguchi, H. Takeda, N. Aota, K. Sunakawa, and Y. Yaguchi, Jpn. J. Appl. Phys. 47, 8506 (2008).
11. N. Ueda, H. Hosono, R. Waseda, and H. Kawazoe, Appl. Phys. Lett. 71, 933 (1997).
12. S. Rafique, L. Han, M. J. Tadjer, J. A. Freitas, Jr., N. A. Mahadik, and H. Zhao, Appl. Phys. Lett. 108, 182105 (2016).
13. H. Okumura, M. Kita, K. Sasaki, A. Kuramata, M. Higashiwaki, and J. S. Speck, Appl. Phys. Express 7, 095501 (2014).
14. Z. Xia, H. Xue, C. Joishi, J. McGlone, N. K. Kalarickal, S. H. Sohel, M. Brenner, A. Arehart, S. Ringel, S. Lodha, W. Lu, and S. Rajan, IEEE Electron Device Lett. 40, 1052 (2019).
15. J. Green, K. D. Chabak, E. R. Heller, R. C. Fitch, Jr., M. Baldini, A. Fiedler, K. Irmscher, G. Wagner, Z. Galazka, S. E. Tetlak, A. Crespo, K. Leedy, and G. H. Jessen, IEEE Electron Device Lett. 37, 902 (2016).
16. M. H. Wong, K. Goto, H. Murakami, Y. Kumagai, and M. Higashiwaki, IEEE Electron Device Lett. 40, 431 (2019).
17. Z. Hu, K. Nomoto, W. Li, N. Tanen, K. Sasaki, A. Kuramata, T. Nakamura, D. Jena, and H. G. Xing, IEEE Electron Device Lett. 39, 869 (2018).
18. K. Konishi, K. Goto, H. Murakami, Y. Kumagai, A. Kuramata, S. Yamakoshi, and M. Higashiwaki, Appl. Phys. Lett. 110, 103506 (2017).
19. C. Joishi, S. Rafique, Z. Xia, L. Han, S. Krishnamoorthy, Y. Zhang, S. Lodha, H. Zhao, and S. Rajan, Appl. Phys. Express 11, 031101 (2018).
20. T. Oshima, T. Okuno, N. Arai, N. Suzuki, S. Ohira, and S. Fujita, Appl. Phys. Express 1, 011202 (2008).
21. N. K. Kalarickal, Z. Feng, A F M A. U. Bhuiyan, Z. Xia, J. F. McGlone, W. Moore, A. R. Arehart, S. A. Ringel, H. Zhao, and S. Rajan, "Electrostatic engineering using extreme permittivity materials for ultra-wide bandgap semiconductor transistors," arXiv preprint arXiv: 2006.02349, 2020.

22. A. Kuramata, K. Koshi, S. Watanabe, Y. Yamaoka, T. Masui, and S. Yamakoshi, Jpn. J. Appl. Phys., Part 1 55, 1202A2 (2016).
23. S. Rafique, M. R. Karim, J. M. Johnson, J. Hwang, H. Zhao, Appl. Phys. Lett. 112, 052104 (2018).
24. H. Murakami, K. Nomura, K. Goto, K. Sasaki, K. Kawara, Q. T. Thieu, R. Togashi, Y. Kumagai, M. Higashiwaki, A. Kuramata, S. Yamakoshi, B. Monemar, and A. Koukitu, Appl. Phys. Express 8, 015503 (2015).
25. R. Schewski, K. Lion, A. Fiedler, C. Wouters, A. Popp, S. V. Levchenko, T. Schulz, M. Schmidbauer, S. Bin Anooz, R. Gruneberg, Z. Galazka, G. Wagner, K. Irmscher, M. Scheffler, C. Draxl, and M. Albrecht, APL Mater. 7, 022515 (2019).
26. P. Mazzolini, A. Falkenstein, C. Wouters, R. Schewski, T. Markurt, Z. Galazka, M. Martin, M. Albrecht, and O. Bierwagen, APL Mater. 8, 011107 (2020).
27. A. Mauze, Y. Zhang, T. Itoh, F. Wu, and J. S. Speck, APL Mater. 8, 021104 (2020).
28. T. S. Ngo, D. D. Le, J. Lee, S.-K. Hong, J.-S. Ha, W.-S. Lee, and Y.-B. Moon, J. Alloys Compd. 834, 155027 (2020).
29. V. G. Hill, R. Roy, and E. F. Osborn, J. Am. Ceram. Soc. 35, 135 (1952).
30. S. Krishnamoorthy, Z. Xia, C. Joishi, Y. Zhang, J. McGlone, J. Johnson, M. Brenner, A. R. Arehart, J. Hwang, S. Lodha, and S. Rajan, Appl. Phys. Lett. 111, 023502 (2017).
31. Y. Zhang, A. Neal, Z. Xia, C. Joishi, J. M. Johnson, Y. Zheng, S. Bajaj, M. Brenner, D. Dorsey, K. Chabak, G. Jessen, J. Hwang, S. Mou, J. P. Heremans, and S. Rajan, Appl. Phys. Lett. 112, 173502 (2018).
32. K. Ghosh and U. Singisetti, J. Mater. Res. 32, 4142 (2017).
33. A F M A. U. Bhuiyan, Z. Feng, J. M. Johnson, Z. Chen, H.-L. Huang, J. Hwang, and H. Zhao, Appl. Phys. Lett. 115, 120602 (2019).
34. P. Ranga, A. Rishinaramangalam, J. Varley, A. Bhattacharyya, D. Feezell, and S. Krishnamoorthy, Appl. Phys. Express 12, 111004 (2019).
35. A F M A. U. Bhuiyan, Z. Feng, J. M. Johnson, H.-L. Huang, J. Sarker, M. Zhu, M. R. Karim, B. Mazumder, J. Hwang, and H. Zhao, APL Mater. 8, 031104 (2020).
36. S. W. Kaun, F. Wu, and J. S. Speck, J. Vac. Sci. Technol. A 33, 041508 (2015).
37. T. Oshima, T. Okuno, N. Arai, Y. Kobayashi, and S. Fujita, Jpn. J. Appl. Phys., Part 1 48, 070202 (2009).
38. A F M A. U. Bhuiyan, Z. Feng, J. M. Johnson, H.-L. Huang, J. Hwang, and H. Zhao, "MOCVD epitaxy of ultra-wide bandgap β-$(Al_xGa_{1-x})_2O_3$ with high-Al composition on (100) β-Ga_2O_3 substrates" 2020 (accepted in ACS Crystal Growth and Design, DOI: 10.1021/acs.cgd.0c00864)
39. H. Peelaers, J. B. Varley, J. S. Speck, and C. G. Van de Walle, Appl. Phys. Lett. 112, 242101 (2018).
40. B. W. Krueger, C. S. Dandeneau, E. M. Nelson, S. T. Dunham, F. S. Ohuchi, and M. A. Olmstead, J. Am. Ceram. Soc. 99 (7), 2467 (2016).
41. M. T. Nichols, W. Li, D. Pei, G. A. Antonelli, Q. Lin, S. Banna, Y. Nishi, and J. L. Shohet, J. Appl. Phys. 115, 094105 (2014).

42. F. Zhang, K. Saito, T. Tanaka, M. Nishio, M. Arita, and Q. Guo, Appl. Phys. Lett. 105, 162107 (2014).
43. Z. Feng, Q. Feng, J. Zhanga, X. Li, F. Li, L. Huang, H.-Y. Chen, H.-L. Lu, and Y. Hao, Appl. Surf. Sci. 434, 440 (2018).
44. C. Fares, F. Ren, E. Lambers, D. C. Hays, B. P. Gila, and S. J. Pearton, J. Vac. Sci. Technol. 36, 061207 (2018).
45. M. A. Khan, M. Shatalov, H. P. Maruska, H. M. Wang and E. Kuokstis, Jpn. J. Appl. Phys., Vol. 44, 7191 (2005).
46. Y.-R. Luo, "Bond Dissociation Energies in CRC Handbook of Chemistry and Physics", 90th ed., edited by D. R. Lide (CRC Press/Taylor and Francis, Boca Raton, 2009).
47. X. Chen, N. Lin, and D. Cai, J. Mater. Res. 28(5), 716 (2013).
48. S. Mu, M. Wang, H. Peelaers, and C. G. Van de Walle, APL Mater. 8, 091105 (2020).
49. T.-C. Wen and W.-I. Lee, Jpn. J. Appl. Phys., Part 1 40, 5302 (2001).

Table Caption

Table 1. Summary of $(\bar{2}01)$ β-$(Al_xGa_{1-x})_2O_3$ samples grown with different [TMAl]/[TMAl + TEGa] molar flow rate ratios, film thicknesses and their corresponding Al compositions and bandgap energies estimated from XRD and XPS characterizations.

Figure Caption

Figure 1 XRD ω-2θ spectra for $(\bar{4}02)$ and $(\bar{6}03)$ reflections from $(\bar{2}01)$ β-$(Al_xGa_{1-x})_2O_3$ films with different Al compositions: 21%, 29%, 36%, 41% and 48%. The $(\bar{4}02)$ and $(\bar{6}03)$ reflections from $(\bar{2}01)$ β-Ga_2O_3 are represented by the high intensity diffraction peaks at $2\theta \approx 38.44°$ and 59.18°, respectively. Blue and green arrow indicate the $(\bar{4}02)$ and $(\bar{6}03)$ reflections of β-$(Al_xGa_{1-x})_2O_3$ films, respectively.

Figure 2 The bandgap energies of $(\bar{2}01)$ β-$(Al_xGa_{1-x})_2O_3$ films determined by the energy difference of O 1s core level peak and the onset of energy loss spectrum for (a) x = 21%, (b) x = 28%, (c) x = 35%, (d) x = 41% and (e) x = 48%.

Figure 3 AFM images (scan area: 5 x 5 μm^2) for $(\bar{2}01)$ β-$(Al_xGa_{1-x})_2O_3$ films grown with Al compositions of (a) x = 21%, (b) x = 29%, (c) x = 41%, and (b) x = 48%. One-dimensional (1D) height profiles showing the maximum height and the length of the granules, are included in inset.

Figure 4 (a) XRD ω-2θ spectra for the $(\bar{6}03)$ reflections of β-$(Al_xGa_{1-x})_2O_3$ films grown with 3.82% of [TMAl]/[TMAl+TEGa] molar flow ratio at different growth conditions: (i) 880°C and 80 torr (red curve), (ii) 920°C and 20 torr (blue curve), and (iii) 880°C and 20 torr (black curve). Surface view FESEM images for the films grown with (ii) and (i) growth conditions are shown in (b) and (c), respectively.

Figure 5 Cross-sectional HAADF-STEM images observed along the [010] zone axis projection for 60 nm thick $(\bar{2}01)$ β-$(Al_{0.48}Ga_{0.55})_2O_3$ film grown on top of $(\bar{2}01)$ β-Ga_2O_3 substrates at (a) low magnification and (b) atomic resolution and associated EDS for (c) Ga and (d) Al. (e) STEM-EDS quantitative line profile displaying the atomic percentage (%) of Al (blue), Ga (green) and O (red) along the $[\bar{2}01]$ direction from the top of the film to the substrate marked with the orange arrow in (a). EDS experimental uncertainty ~ ±5%.

Figure 6 Cross-sectional HAADF-STEM images of the 8-period $(\bar{2}01)$ β-$(Al_{0.48}Ga_{0.52})_2O_3$/β-$Ga_2O_3$ superlattice structure grown on $(\bar{2}01)$ β-Ga_2O_3 substrate at (a) low magnification and (b) atomic resolution and associated EDS maps for (c) Ga and (d) Al. (e) STEM-EDS line profile displaying the atomic percentage (%) of Al (blue), Ga (green) and O (red) along the $[\bar{2}01]$ direction marked with the orange arrow in (a). EDS experimental uncertainty ~ ±5%.

Table 1

Sample No	[TMAl]/[TMAl +TEGa] (%)	Film Thickness (nm)	Al composition (XRD) (%)	Al composition (XPS) (%)	Bandgap energies (eV)
1	2.35	~155	21	20.58	5.20 ± 0.06
2	3.82	~173	29	28.10	5.35 ± 0.04
3	7.27	~167	36	35.23	5.44 ± 0.08
4	10.36	~177	41	41.48	5.54 ± 0.05
5	18.08	~197	48	47.94	5.72 ± 0.08

Figure 1

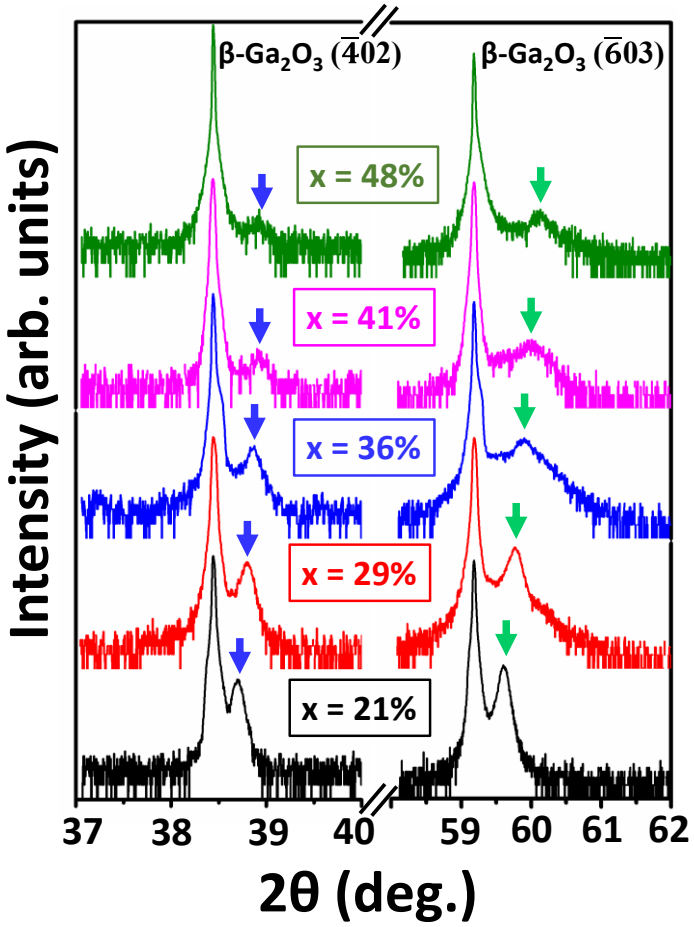
β-Ga2O3 (4̄02)
β-Ga2O3 (6̄03)
x = 48%
x = 41%
x = 36%
x = 29%
x = 21%
Intensity (arb. units)
37
38
39
40
59
60
61
62
2θ (deg.)

Figure 2

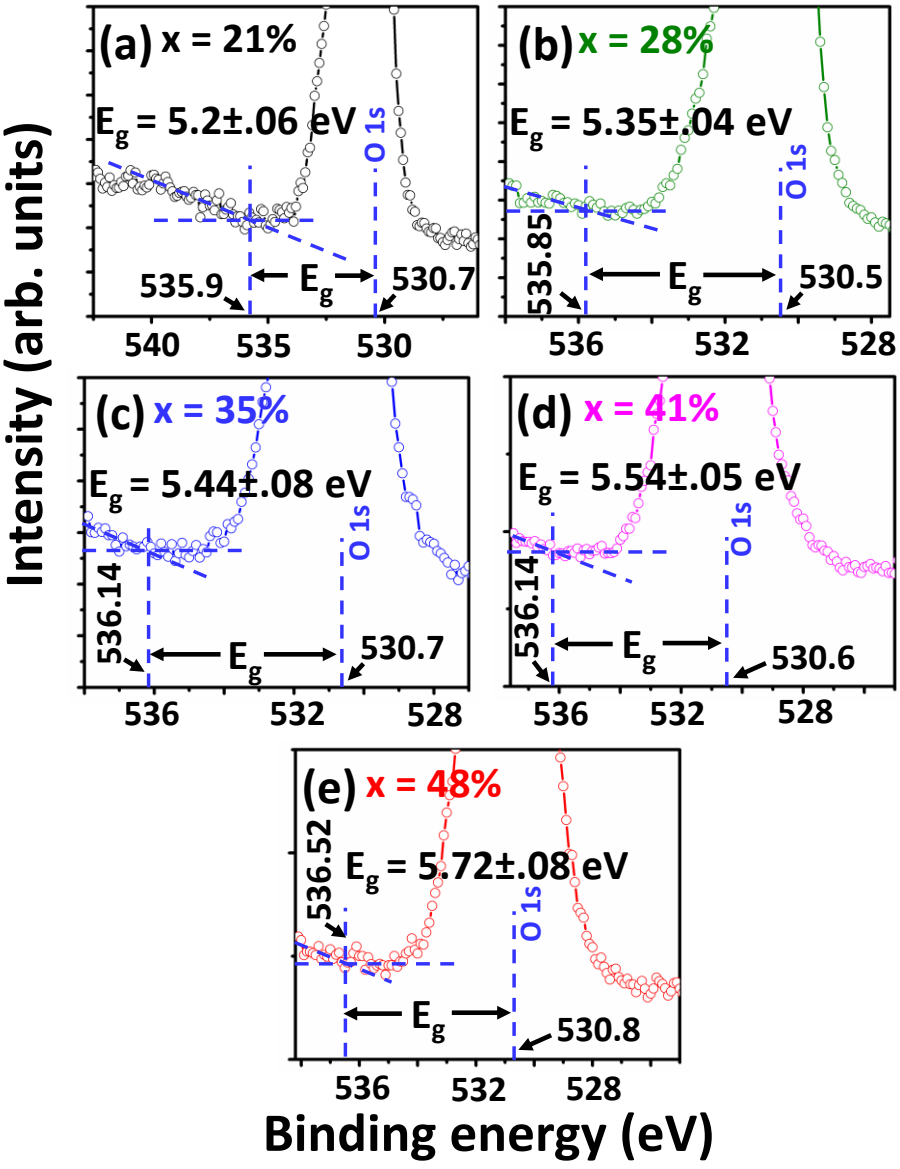
(a) x = 21%
E_g = 5.2±.06 eV
O 1s
535.9
E_g
530.7
540
535
530
(b) x = 28%
E_g = 5.35±.04 eV
O 1s
535.85
E_g
530.5
536
532
528
(c) x = 35%
E_g = 5.44±.08 eV
O 1s
536.14
E_g
530.7
536
532
528
(d) x = 41%
E_g = 5.54±.05 eV
O 1s
536.14
E_g
530.6
536
532
528
(e) x = 48%
536.52
E_g = 5.72±.08 eV
O 1s
E_g
530.8
536
532
528
Intensity (arb. units)
Binding energy (eV)

Figure 3

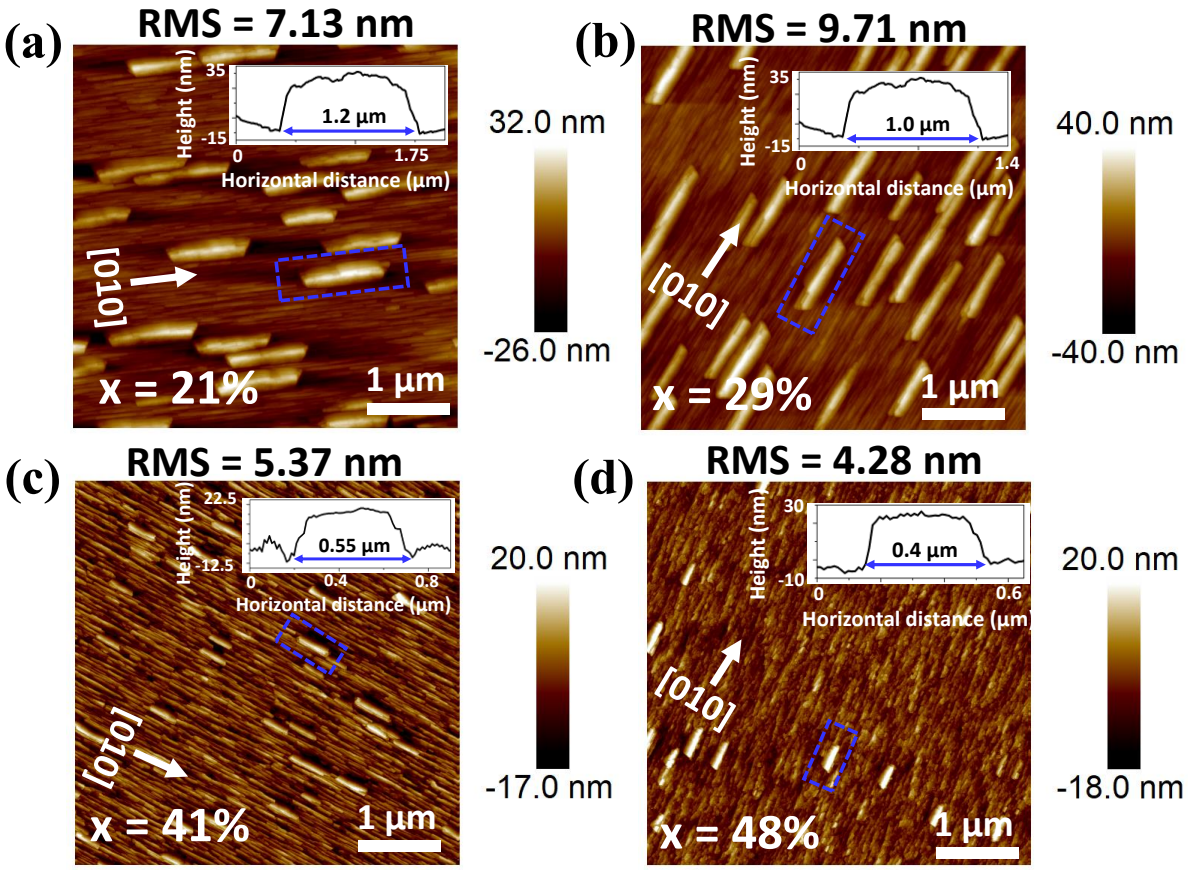
(a)
RMS = 7.13 nm
Height (nm)
35
-15
1.2 µm
0
1.75
Horizontal distance (µm)
[010]
x = 21%
1 µm
32.0 nm
-26.0 nm
(b)
RMS = 9.71 nm
Height (nm)
35
-15
1.0 µm
0
1.4
Horizontal distance (µm)
[010]
x = 29%
1 µm
40.0 nm
-40.0 nm
(c)
RMS = 5.37 nm
Height (nm)
22.5
-12.5
0.55 µm
0
0.4
0.8
Horizontal distance (µm)
[010]
x = 41%
1 µm
20.0 nm
-17.0 nm
(d)
RMS = 4.28 nm
Height (nm)
30
-10
0.4 µm
0
0.6
Horizontal distance (µm)
[010]
x = 48%
1 µm
20.0 nm
-18.0 nm

Figure 4

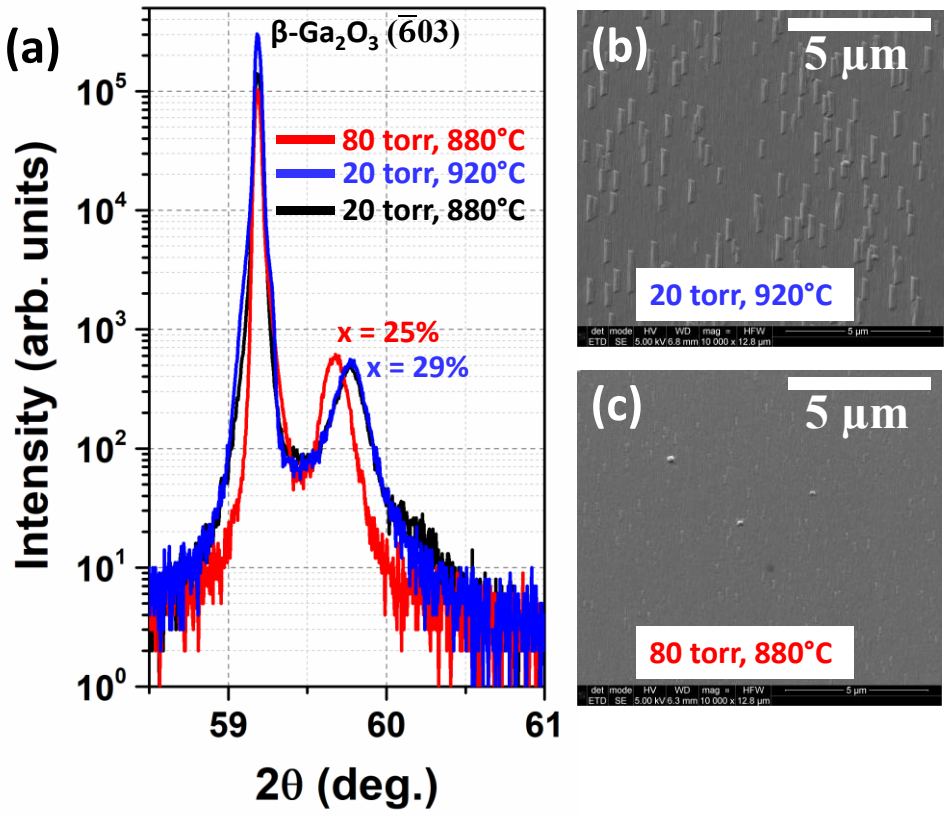
(a)
β-Ga2O3 (603)
80 torr, 880°C
20 torr, 920°C
20 torr, 880°C
x = 25%
x = 29%
Intensity (arb. units)
2θ (deg.)
(b)
5 µm
20 torr, 920°C
(c)
5 µm
80 torr, 880°C

Figure 5

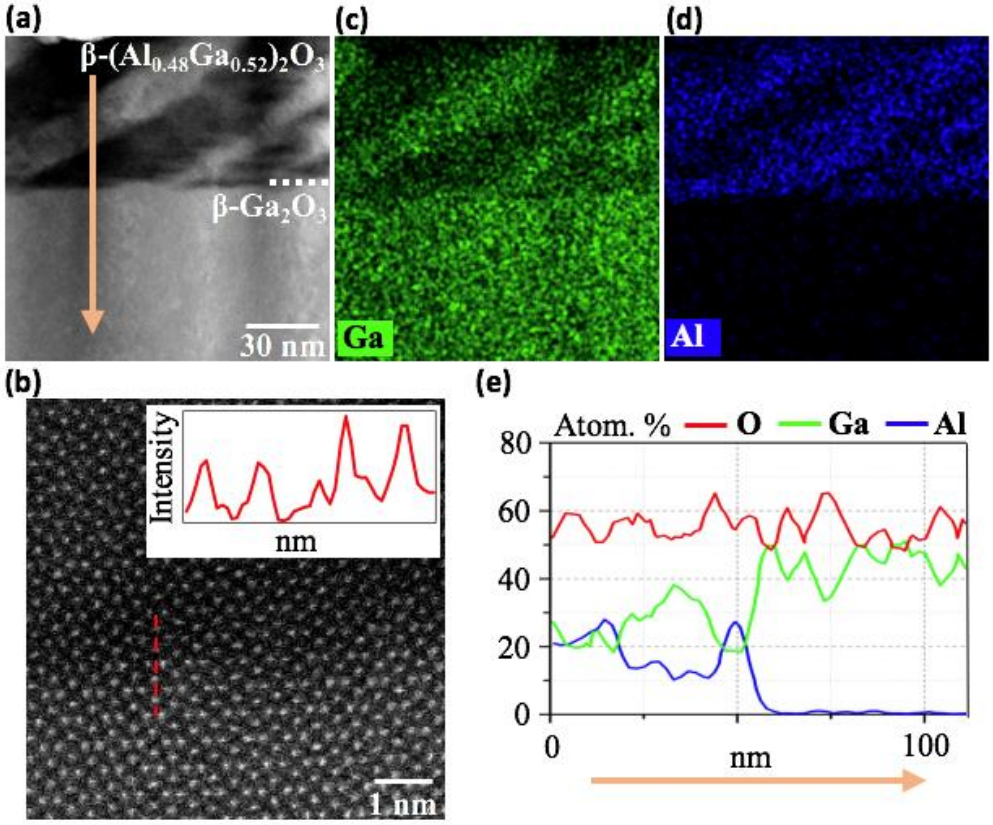
(a)
β-(Al0.48Ga0.52)2O3
β-Ga2O3
30 nm
(c)
Ga
(d)
Al
(b)
Intensity
nm
1 nm
(e)
Atom. %
O
Ga
Al
80
60
40
20
0
0
nm
100

Figure 6

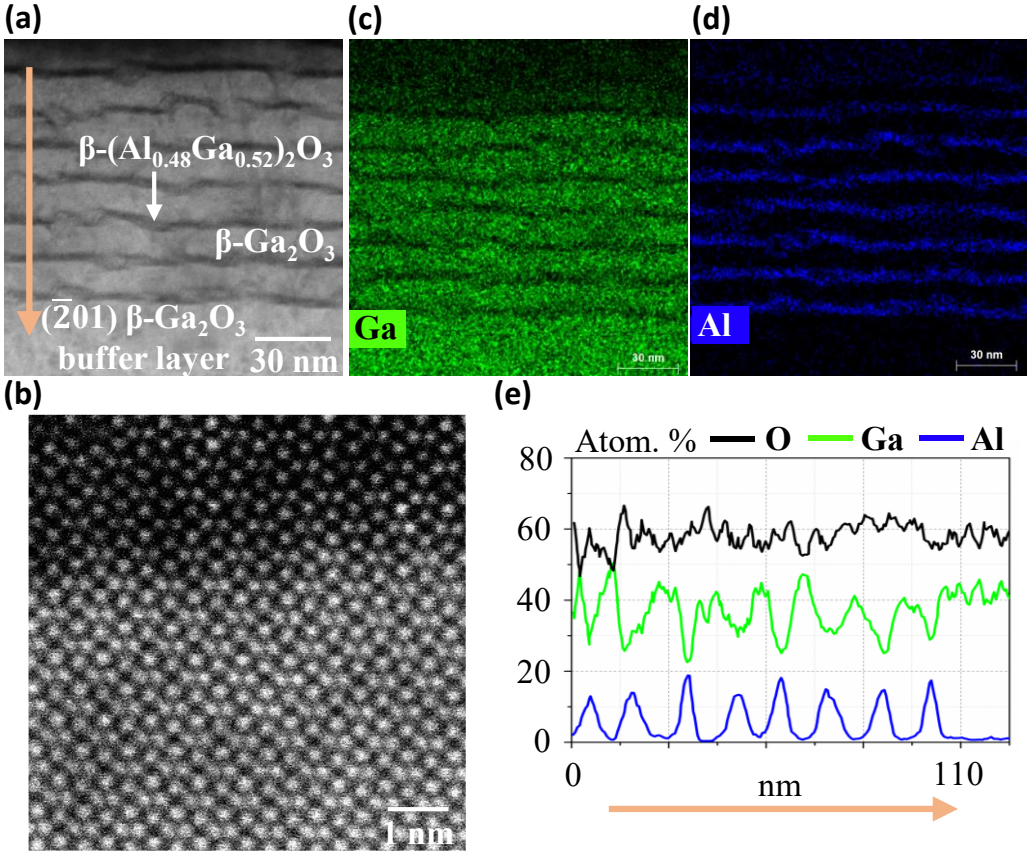
(a)
β-(Al0.48Ga0.52)2O3
β-Ga2O3
(2̄01) β-Ga2O3
buffer layer
30 nm
(c)
Ga
30 nm
(d)
Al
30 nm
(b)
1 nm
(e)
Atom. %
O
Ga
Al
80
60
40
20
0
0
nm
110